Optica Applicata, Vol. LIV, No. 3, 2024
DOI: 10.37190/oa240303

Research on a highly sensitive surface plasmon resonance sensor based on side-polished holey fiber with circle lattice

Jian-Fei Liao

School of Mechanical and Electrical Engineering, Wuyi University, Wuyishan 354300, China:
e-mail: jfliao@126.com

Using the strong local electromagnetic field enhancement of surface plasmon polaritons (SPP), a highly sensitive surface plasmon resonance (SPR) sensor based on side-polished circle lattice holey fiber (HF) is proposed. The coupling resonance properties of the sensor are numerically studied, and the investigation findings indicate that our proposed sensor can realize single-resonance detection within a wide wavelength range of 1.189–1.921 μm for the refractive index (RI) of the analyte changes from 1.28 to 1.39. The highest wavelength sensitivity, amplitude sensitivity, and RI resolution are up to 21,400 nm/RIU, 363.4 RIU^{-1}, and 4.67×10^{-6} RIU, respectively. Therefore, our proposed sensor will have broad application prospects in RI sensing, including water pollution monitoring, medical treatment, and food safety detection.

Keywords: fiber optics, holey fiber, surface plasmon resonance, sensor.

1. Introduction

In recent years, optical sensors based on surface plasmon resonance (SPR) have been widely investigated and applied in disease detection [1-3], chemical reaction monitoring [4], biochemical research [5], and other photonic devices [6, 7] thanks to their unique and excellent capabilities including high detectable sensitivity, online, and label -free measurement. However, most optical SPR sensors, which contain a coupling prism structure [8, 9], have several limitations, such as high cost, bulky configuration, unsuitability for distributed sensing, etc. To solve these defects, optical fiber is used to displace the bulky prism since it is more flexible and can increase system integration [10-14]. Moreover, SPR-based optical fiber sensors have become more appealing due to their advantages such as anti-electromagnetic interference, mechanical stability, and higher sensing capability [15]. Nevertheless, the coupling condition between the plasmonic and fiber core modes is always hard to satisfy because the refractive index (RI) values of these two modes are usually unequal.

With the aim of solving the phase matching issues of SPR optical fiber sensors, SPR holey fiber (HF) sensors have been proposed thanks to their flexible design structure [16-18]. But the traditional SPR HF sensors are devised by selectively filling the air holes with an inside metal coating method [19, 20]. This type of SPR-based HF sensor is always hard to implement practically. Hence, various practically realizable SPR-based HF sensors have been designed by placing the analyte and metal coating layer outside of HF recently [21-28]. In 2018, a SPR sensor was developed by CHAKMA *et al.* using a circular layer of HF [21]. Benefiting from locating the sensing media outside of HF, the highest wavelength and amplitude sensitivities were 9000 nm/refractive index unit (RIU) and 318 RIU^{-1}, respectively. Furthermore, the index resolution was up to 1.11×10^{-5} when the RI of the analyte lay in (1.34, 1.37). In the same year, TONG *et al.* proposed an SPR sensor utilizing three-core HF [22]. The gold film is placed outside of HF while the sensing media is lying on the gold layer surface. Their findings showed that a change in analyte RI from 1.33 to 1.40 resulted in an average wavelength sensitivity of 3435 nm/RIU and the highest resolution of 2.91×10^{-6} RIU. An H-shaped HF SPR sensor was developed by LI *et al.* in 2020 was intended for RI detection [23]. Thanks to its U-shaped groove open structure, the highest sensitivity to wavelength in the sensor design was 12,600 nm/RIU when the analyte RI lay in (1.33, 1.41). Moreover, a new type of SPR sensor that grounded on dual-side polished HF with a twin-core was developed by HAN *et al.* [24]. Based on the simulation results, an extensive sensing range of 1.35–1.47 achieved the highest wavelength sensitivity of 20700 nm/RIU, and the highest recorded amplitude sensitivity was up to 1479.03 RIU^{-1}. However, sensitivities of 1800 nm/RIU for wavelength and 73.6 RIU^{-1} for amplitude achieved at the low detection range of 1.35–1.39. In 2021, WANG *et al.* developed a trapezium-shaped groove HF SPR sensor for low RI sensing [26]. Following the adjustment of the sensing range to 1.18–1.3, the highest sensitivity of 9100 nm/RIU for wavelength was obtained. Moreover, the highest amplitude sensitivity and RI resolution were 99 RIU^{-1} and 1.10×10^{-5}, respectively. In 2022, a side-opening HF SPR sensor was proposed for RI and temperature detection [27]. When the sensing range changed from 1.33 to 1.34, the highest wavelength and temperature sensitivities were 1488 nm/RIU and 527.2 pm/°C, correspondingly. Additionally, some SPR sensors based on photonic quasi-crystal fibers have also been proposed for RI sensing. For example, LIU *et al.* proposed a new type of SPR sensor using an eccentric core photonic quasi-crystal fiber [28]. the highest wavelength sensitivity was up to 21,100 nm/RIU when the analyte RI lay in (1.33, 1.39). CHU *et al.* designed a high RI detection SPR sensor using photonic quasi-crystal fiber [29]. Their findings indicated that the highest wavelength sensitivity of 17,000 nm/RIU was achieved for the detection range of 1.44–1.57. In 2023, MANICKAM *et al.* proposed a photonic quasi-crystal fiber SPR sensor for urinary methanol sensing [30]. With RI lying in the range of 1.32–1.36, the highest values for wavelength sensitivity, amplitude sensitivity, and figure of merit are 5000 nm/RIU, 150 RIU^{-1}, and 163.09, respectively.

In this paper, a highly sensitive SPR sensor based on a circle lattice HF coated with indium tin oxide (ITO) is proposed for low RI sensing. With a dual-side polished structure, efficient enhancement of coupling intensity between plasmonic and fiber core modes is achievable. The detection property is numerically discussed thoroughly. The findings indicate that the highest wavelength and amplitude sensitivities are as high as 21400 nm/RIU and 363.4 RIU^{-1}, respectively. Meanwhile, the highest RI resolution of 4.67×10^{-6} RIU is obtained with the instrument's resolution of 0.1 nm.

2. Structure design and theoretical model

The geometry of our proposed SPR sensor, which utilizes an ITO-coated HF, is illustrated in Fig. 1. To simplify the sensor fabrication, the HF cladding region has only two layers of air holes arranged in a circular lattice. The single core is formed by replacing one silica rod with an air hole at the center of HF. In addition, both sides of HF, which are coated with ITO film, are polished to generate the SPR effect efficiently. Our proposed sensor is less expensive and simpler in structure than other SPR sensors adopting a dual-side polished gold-coated HF [24,25]. The sensor parameters are the inner and outer ring air hole pitch R_1, R_2, air hole diameter d_1, d_2, d_3, ITO layer thickness t, and spacing from the fiber central l. The analyte RI is n_a. The RI of the background materials can be obtained from the Sellmeier equation [31], while the permittivity of ITO is calculated from the Drude model [31]. Note that the circle lattice HF can be produced through the stack-and-draw technique, and the dual-side polished structure can be accomplished by using a 3D mechanical platform with a wheel-polishing setup. Moreover, we can adopt the chemical deposition technique to deposit ITO film.

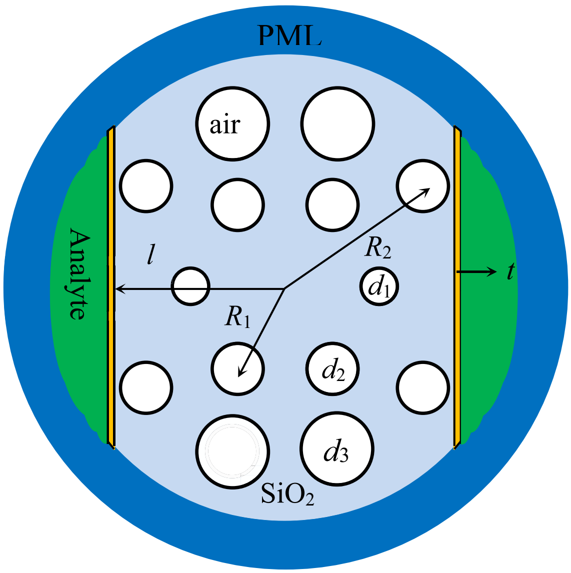

Fig. 1. The structure of the proposed HF-SPR sensor.

To evaluate the sensor's detection quality comprehensively, we study the loss CL, wavelength sensitivity S_λ and amplitude sensitivity S_a by using the following equations [31]

$$\mathrm{CL}(\mathrm{dB/cm}) = 8.686 \times \frac{2\pi}{\lambda}\mathrm{Im}(n_{\mathrm{eff}}) \times 10^4 \tag{1}$$

$$S_\lambda(\mathrm{nm/RIU}) = \frac{\Delta\lambda_{\mathrm{peak}}(n_a)}{\Delta n_a} \tag{2}$$

$$S_a = -\frac{\Delta\mathrm{CL}/\Delta n_a}{\mathrm{CL}_{\mathrm{initial}}} \tag{3}$$

where λ and $\mathrm{Im}(n_{\mathrm{eff}})$ indicate the working wavelength and the imaginary part of the n_{eff}, respectively. $\Delta\lambda_{\mathrm{peak}}$ indicates the modification of peal wavelength. Δn_a is the variation of n_a. ΔCL denotes the loss variation, while $\mathrm{CL}_{\mathrm{initial}}$ stands for the loss in the original state.

3. Simulation results and discussions

Based on the full-vector FEM [32], the *E*-field profiles of the sensor at the wavelengths 1.45, 1.60 and 1.75 μm, which are shown in Fig. 2, are numerical studied with the HF parameters $R_1 = 3.1$ μm, $R_2 = 5.0$ μm, $d_1 = 0.4$ μm, $d_2 = 0.6$ μm, $d_3 = 0.9$ μm, $t = 60$ nm, $l = 5.0$ μm, $n_a = 1.37$.In Figs. 2(g), (h) and (i), one can observe that throughout the operating wavelength range, the field distribution of the *y*-polarized

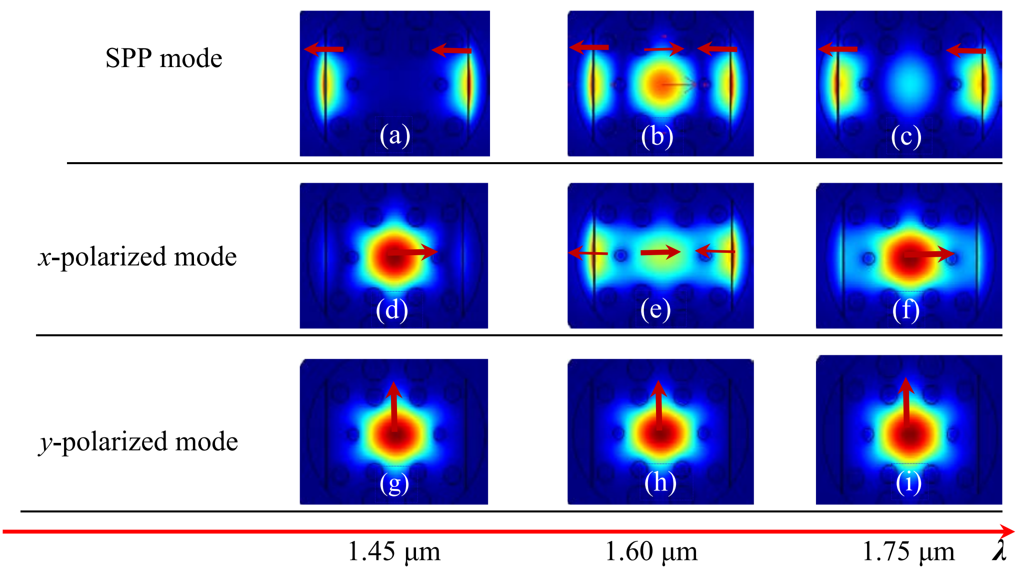

Fig. 2. Distributions of electric fields for the SPP mode, *x*-polarized and *y*-polarized modes.

fundamental mode is parallel to the ITO layer surface, resulting in minimal coupling with SPP mode and mainly existing in the core region. This coupling property can protect the sensor from the crossing interference generated by multimode resonance [22-24]. Hence, only the coupling property of the x-polarized fundamental mode is studied in this work. According to Figs. 2(a) and (d), we can learn that the x-polarized and SPP modes state in a weak-coupling situation at 1.45 μm. However, when the resonance condition between the x-polarized and SPP modes is met at 1.60 μm, the majority of the E-field energy is transferred from the former to the latter, which are illustrated in Figs. 2(b) and (e). According to Figs. 2(c) and (f), the coupling strength between the x-polarized fundamental and SPP modes becomes weak again at 1.75 μm since these two modes no longer meet the resonance condition.

The mode resonance properties are also studied by keeping the HF parameters unchanged, and the simulation results are given in Fig. 3. In Fig. 3(a), the values of $\mathrm{Re}(n_y)$ decrease gradually if the operation wavelength varies from 1.45–1.75 μm. On the other hand, the values of $\mathrm{Re}(n_{\mathrm{spp}})$ are larger than that of $\mathrm{Re}(n_x)$ in the short-wavelength range, which leads the coupling strength between these two modes to become weak. But at the resonance point, the values of $\mathrm{Re}(n_x)$ and $\mathrm{Re}(n_{\mathrm{spp}})$ are equal. It indicates that the point at which resonance occurs between these two modes is met at 1.60 μm. Moreover, after the resonance point, the values of $\mathrm{Re}(n_x)$ enlarge abruptly while the values of $\mathrm{Re}(n_{\mathrm{spp}})$ suddenly reduce. This is because the phase of these two modes is impacted severely when the SPR effect happens. Fig. 3(b) gives the loss curves. The loss of the y-polarized fundamental mode (CL_y) is really small and remains almost unchanged for increasing the wavelength from 1.45 to 1.75 μm. This is because y-polarized and SPP modes exhibit a weak intensity of interaction, which is verified by the E-field profiles shown in Fig. 2. Unlike the CL_y, the loss of the x-polarized mode (CL_x) rises and then falls. Meanwhile, the loss of the SPP mode ($\mathrm{CL}_{\mathrm{spp}}$) rises and then falls, then increases again with the increment of the wavelength. However, CL_x and $\mathrm{CL}_{\mathrm{spp}}$ have identical values at the resonance point. It implies that our proposed sensor can achieve fully-coupled resonance, which can make the sensor more sensitive.

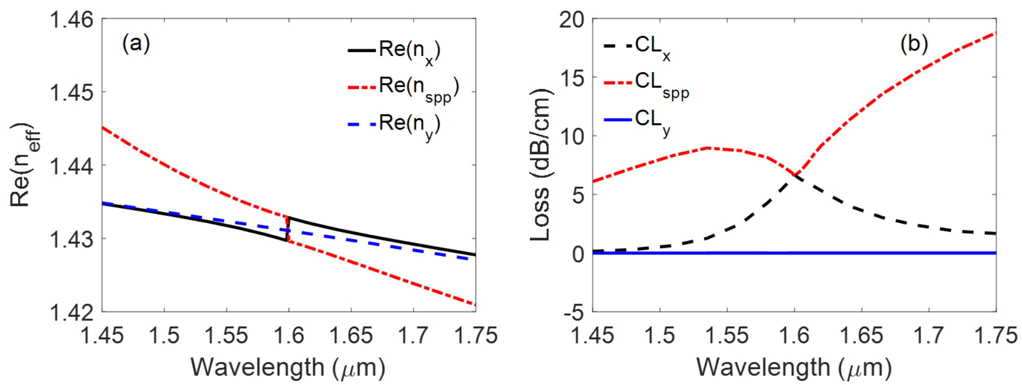

Fig. 3. The dispersion curve (a) and loss curve (b) of the sensor.

With the HF parameters $R_1 = 3.1$ μm, $R_2 = 5$ μm, $d_1 = 0.4$ μm, $d_2 = 0.6$ μm, $d_3 = 0.9$ μm, and $l = 5$ μm, we investigate the effects of t and n_a on the resonant properties, and the findings are displayed in Fig. 4. According to Fig. 4(a), the resonant wavelength experiences a red shift for $n_a = 1.37$ as the value of t ranges from 50 to 70 nm. For instance, the value of the peak wavelength for $t = 50$ nm is 1.462 μm while the value of the resonant wavelength is up to 1.739 μm for $t = 70$ nm. It can be attributed to that a larger t causes a greater distance between the ITO surface and HF core region, and results in that the interaction between the x-polarized and SPP modes is limited to the longer wavelength region. Fig. 4(b) depicts the impact of n_a on the resonance wavelength for the ITO film with a thickness of 50–70 nm. If the ITO film's thickness keeps unchanged, the peak wavelength increases quickly within n_a rising from 1.28 to 1.39. It is worth noting that when $t = 70$ nm, the x-polarized mode can not couple with the SPP mode at $n_a = 1.39$, and the peak wavelength can be as short as 1.305 μm for $n_a = 1.28$ when the peak wavelength is as long as 1.901 μm for $n_a = 1.38$. Otherwise, the increased speed of the peak wavelength with the high sensing RI is higher than that of the low detection RI. Such as at $n_a = 1.39$, the resonance wavelength at t ranging

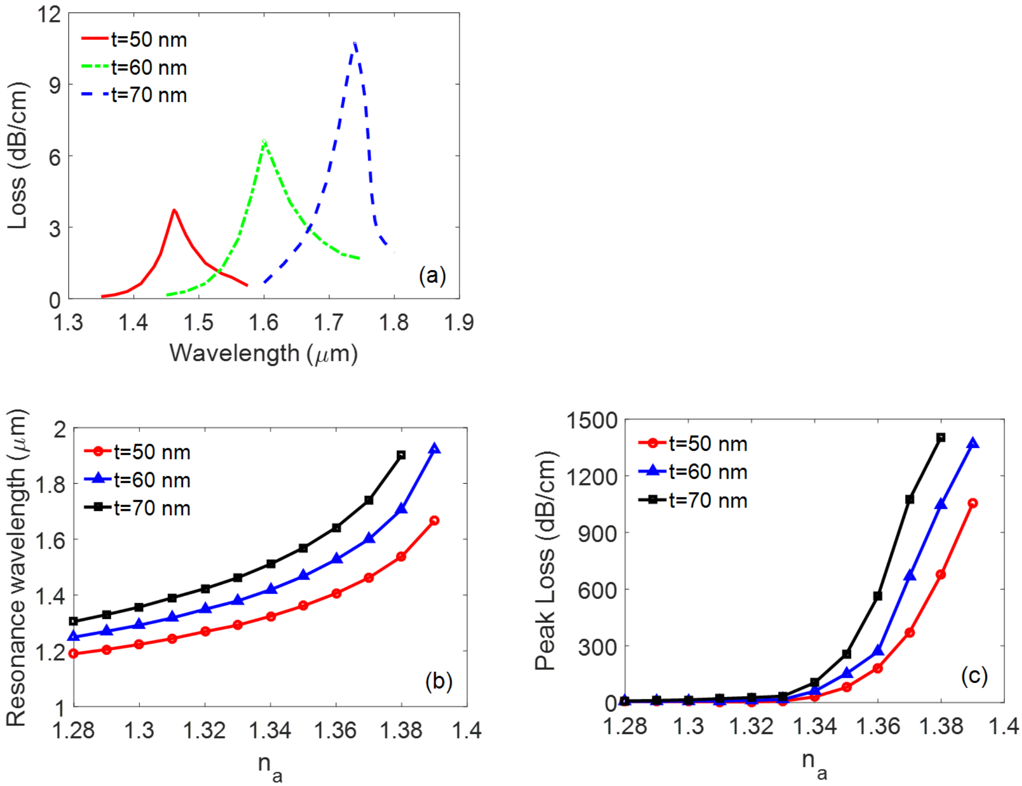

Fig. 4. (a) The influence of t on the loss curve of the x-polarized mode at $n_a = 1.37$; (b) the impact of n_a on the peak wavelength for $t = 50$, 60, 70 nm; (c) the effect of n_a on the peak loss for $t = 50$, 60, 70 nm.

from 50 to 60 nm increases from 1.666 to 1.921 μm. But if $n_a = 1.28$, the resonance wavelength rises only from 1.189 μm to 1.249 μm when t changes from 50 to 60 nm. The reason is that a higher n_a causes to a higher $\mathrm{Re}(n_{spp})$ while $\mathrm{Re}(n_x)$ almost keeps unchanged. Therefore, the peak wavelength has a red shift. The effect of n_a on the peak loss for $t = 50$, 60, and 70 nm is given in Fig. 4(c). As t remains unchanged, the peak loss increases slowly with n_a varying from 1.28 to 1.33 while the peak loss increases quickly with n_a varying from 1.33 to 1.39. The reason is that the coupling intensity between these two modes is too weak when n_a lies in (1.28, 1.33). However, the interaction intensity between these two modes can be significantly increased by adjusting n_a between 1.33 and 1.39, and then the E-field energy transferred to the SPP mode increases as a result of transfer from the fiber core mode. However, if n_a remains unchanged, the peak loss increases with t adjusting from 50 to 70 nm. It occurs due to the increased resonant intensity as t rises from 50 to 70 nm.

To examine the sensor's detection quality, the wavelength and amplitude sensitivities were analyzed, taking into account the impact of t and n_a, the findings are presented in Fig. 5. The HF parameters are $R_1 = 3.1$ μm, $R_2 = 5$ μm, $d_1 = 0.4$ μm, $d_2 = 0.6$ μm, $d_3 = 0.9$ μm, and $l = 5$ μm. Figure 5(a) displays that S_λ rises with n_a changing from 1.28–1.29, 1.29–1.30, 1.30–1.31, 1.31–1.32, 1.32–1.33, 1.33–1.34, 1.34–1.35, 1.35 –1.36, 1.36–1.37, 1.37–1.38 and 1.38–1.39 when $t = 50$, 60 nm, respectively. Particularly at $t = 60$ nm, is only 2100 nm/RIU as n_a adjusts from 1.28 to 1.29. But if n_a varies from 1.38–1.39, S_λ is up to 21400 nm/RIU. Moreover, the wavelength sensitivities of 2500, and 17200 nm/RIU are obtained at $t = 70$ nm when n_a changes from 1.28–1.29, and 1.37–1.38 correspondingly. Hence, the upper limit of resolution is 4.67×10^{-6} RIU when the instrument's resolution is 0.1 nm. In addition, if n_a keeps invariable, S_λ increases with t enhancing from 50 to 70 nm. Figure 5(b) shows the impacts of t and n_a on S_a. As t remains unchanged, S_a increases with n_a varying from 1.28 to 1.33 while decreases with n_a varying from 1.33 to 1.38. On the contrary, if n_a lies in (1.32, 1.38), S_a is inversely proportional to the t, and the highest S_a of 363.4 RIU^{-1} is realized for

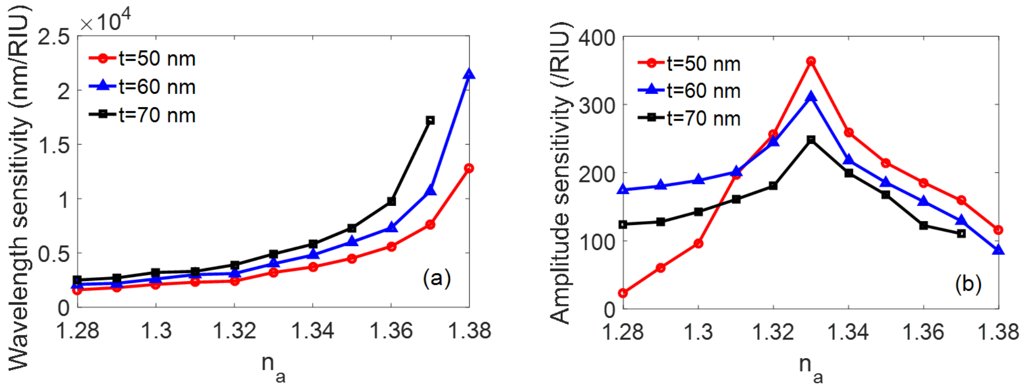

Fig. 5. The effect of n_a on the wavelength sensitivity (a) and amplitude sensitivity (b) when $t = 50, 60, 70$ nm.

T a b l e. Evaluating the performance of other HF-SPR sensors comparatively.

Fiber structure	RI range [RIU]	Max. wavelength sensitivity [nm/RIU]	Max. amplitude sensitivity [RIU^{-1}]	Ref.
D-shaped HF	1.28–1.34	6000	148	[31]
Hollow-core D-shaped HF	1.33–1.34	2900	120	[34]
Dual-core dual-side polished HF	1.35–1.47	20700	1479.03	[24]
Au-based three-core HF	1.33–1.40	3435	N/A	[22]
Elliptical-lattice polished HF	1.395–1.415	12400	252	[33]
Trapezium-shaped groove HF	1.18–1.30	9100	99	[26]
H-shaped HF	1.33–1.41	12600	56.37	[23]
Side-opening HF	1.33–1.34	1488	N/A	[27]
This work	1.28–1.39	21400	363.4	N/A

$t = 50$ nm when n_a changes from 1.33 to 1.34. Therefore, our proposed sensor with excellent sensing performance is very suitable for RI detection.

For the purpose of comparing with other HF-SPR sensors, the Table generalizes the sensing performances of these SPR-HF sensors by placing the analyte and metal coating layer outside of HF. It can be learn from this Table that the highest wavelength and amplitude sensitivities of our developed sensor are much higher than that of other HF-SPR sensors except the dual-side polished HF SPR sensor [24]. However, these dual-side polished HF SPR sensors are more suitable for high RI detection since their sensing performances are not good enough in case the analyte's RI is under 1.39. Consequently, our proposed sensor has great potential applications for low RI sensing.

4. Conclusions

A high-sensitivity SPR sensor based on side-polished HF with a circle lattice is introduced for low RI sensing. In order to realize the SPR effect in the proposed sensor, ITO is adopted as a plasmonic material coated on two polished surfaces of HF. The side -polished ITO-coated fiber structure can not only improve the detection sensitivity by strengthening the interaction intensity between the *x*-polarized and SPP modes, but also can greatly reduce the difficulty of ITO coating and make the sensor easy to fabricate. By using the full-vector FEM, the sensing characteristics are numerically investigated thoroughly. The findings manifest that complete coupling can be realized. Additionally, the sensing performances can be effectively influenced by the sensor parameters. The highest S_λ, S_a and resolution are as high as 21,400 nm/RIU, 363.4 RIU^{-1} and 4.67×10^{-6} RIU, respectively. These findings provide a reference for the RI detection including water pollution monitoring, chemical, and biological sensing.

Acknowledgment

This work was supported by the Natural Science Foundation of Fujian Province of China (Grand No. 2022J011193), the Science and Technology Program of Nanping of China (Grand No. N2021J001) and the Scientific Research Foundation for the Wuyi University (Grant No. YJ202104).

References

[1] Ramola A., Marwaha A., Singh S., *Design and investigation of a dedicated PCF SPR biosensor for CANCER exposure employing external sensing*, Applied Physics A **127**(9), 2021: 643. https://doi.org/10.1007/s00339-021-04785-2

[2] Yasli A., *Cancer detection with surface plasmon resonance-based photonic crystal fiber biosensor*, Plasmonics **16**, 2021: 1605-1612. https://doi.org/10.1007/s11468-021-01425-6

[3] Natesan A., Govindasamy K.P., Gopal T.R., Dhasarathan V., Aly A.H., *Tricore photonic crystal fibre based refractive index sensor for glucose detection*, IET Optoelectronics **13**(3), 2019: 118-123. https://doi.org/10.1049/iet-opt.2018.5079

[4] Zhao Y., Lei M., Liu S.X., Zhao Q., *Smart hydrogel-based optical fiber SPR sensor for pH measurements*, Sensors and Actuators B: Chemical **261**, 2018: 226-232. https://doi.org/10.1016/j.snb.2018.01.120

[5] Dash J.N., Jha R., *On the performance of graphene-based D-shaped photonic crystal fibre biosensor using surface plasmon resonance*, Plasmonics **10**(5), 2015: 1123-1131. https://doi.org/10.1007/s11468-015-9912-7

[6] Wang Y., Qin F., Yi Z., Chen X., Zhou Z., Yang H., Liao X., Tang Y., Yao W., Yi Y., *Effect of slit width on surface plasmon resonance*, Results in Physics **15**, 2019: 102711. https://doi.org/10.1016/j.rinp.2019.102711

[7] Yu P., Chen X., Yi Z, Tang Y., Yang H., Zhou Z., Duan T., Cheng S., Zhang J., Yi Y., *A numerical research of wideband solar absorber based on refractory metal from visible to near infrared*, Optical Materials **97**, 2019: 109400. https://doi.org/10.1016/j.optmat.2019.109400

[8] Singh P., *SPR biosensors: Historical perspectives and current challenges*, Sensors and Actuators B: Chemical **229**, 2016: 110-130. https://doi.org/10.1016/j.snb.2016.01.118

[9] Masson J.F., *Portable and field-deployed surface plasmon resonance and plasmonic sensors*, Analyst **145**(11), 2020: 3776-3800. https://doi.org/10.1039/D0AN00316F

[10] Tubb A.J.C., Payne F.P., Millington R.B., Lowe, C.R., *Single-mode optical fiber surface plasma wave chemical sensor*, Sensors and Actuators B: Chemical **41**(1-3), 1997: 71-79. https://doi.org/10.1016/S0925-4005(97)80279-1

[11] Peng W., Banerji S., Kim Y.C., Booksh K.S., *Investigation of dual-channel fiber-optic surface plasmon resonance sensing for biological applications*, Optics Letters **30**(22), 2005: 2988-2990. https://doi.org/10.1364/OL.30.002988

[12] Špačková B., Homola J., *Theoretical analysis of a fiber optic surface plasmon resonance sensor utilizing a Bragg grating*, Optics Express **17**(25), 2009: 23254-23264. https://doi.org/10.1364/OE.17.023254

[13] Santos D.F., Guerreiro A., Baptista J.M., *Surface plasmon resonance sensor based on D-type fiber with a gold wire*, Optik **139**, 2017: 244-249. https://doi.org/10.1016/j.ijleo.2017.03.035

[14] Navarrete M.C., Díaz-Herrera N., González-Cano A., Esteban Ó., *Surface plasmon resonance in the visible region in sensors based on tapered optical fibers*, Sensors and Actuators B: Chemical **190**, 2014: 881-885. https://doi.org/10.1016/j.snb.2013.09.066

[15] Gandhi M.S.A., Chu S., Senthilnathan K., Babu P.R., Nakkeeran K., Li Q., *Recent advances in plasmonic sensor-based fiber optic probes for biological applications*, Applied Sciences **9**(5), 2019: 949. https://doi.org/10.3390/app9050949

[16] Islam M.S., Paul B.K., Ahmed K., Asaduzzaman S., *Rhombic core photonic crystal fiber for sensing applications: Modeling and analysis*, Optik **157**, 2018: 1357-1365. https://doi.org/10.1016/j.ijleo.2017.12.048

[17] Karim M.S., Hossin S., Alam M.R., Siddik M.A.B., Aktar M.R., Ahmed N., Shakh M.A.N., *Quad core gold coated photonic crystal fiber temperature sensor based on surface plasmon resonance*, Sensing and Bio-Sensing Research **39**, 2023: 100548. https://doi.org/10.1016/j.sbsr.2022.100548

[18] Liu C, Su W, Liu Q, Lu X., Wang F., Sun T., Chu P.K., *Symmetrical dual D-shape photonic crystal fibers for surface plasmon resonance sensing*, Optics Express **26**(7), 2018: 9039-9049. https://doi.org/10.1364/OE.26.009039

[19] RIFAT A.A., MAHDIRAJI G.A., CHOW D.M., SHEE Y.G., AHMED R., ADIKAN F.R.M., *Photonic crystal fiber-based surface plasmon resonance sensor with selective analyte channels and graphene-silver deposited core*, Sensors **15**(5), 2015: 11499-11510. https://doi.org/10.3390/s150511499

[20] DASH J.N., JHA R., *SPR biosensor based on polymer PCF coated with conducting metal oxide*, IEEE Photonics Technology Letters **26**(6), 2014: 595-598. https://doi.org/10.1109/LPT.2014.2301153

[21] CHAKMA S., KHALEK M.A., PAUL B.K., AHMED K., HASAN M.R., BAHAR A.N., *Gold-coated photonic crystal fiber biosensor based on surface plasmon resonance: design and analysis*, Sensing and Bio-Sensing Research **18**, 2018: 7-12. https://doi.org/10.1016/j.sbsr.2018.02.003

[22] TONG K., WANG F., WANG M., DANG P., WANG Y., *Three-core photonic crystal fiber surface plasmon resonance sensor*, Optical Fiber Technology **46**, 2018: 306-310. https://doi.org/10.1016/j.yofte.2018.11.014

[23] LI T, ZHU L, YANG X, LUO X., YU L., *A refractive index sensor based on H-shaped photonic crystal fibers coated with Ag-graphene layers*, Sensors **20**(3), 2020: 741. https://doi.org/10.3390/s20030741

[24] HAN H., HOU D., LUAN N., BAI Z., SONG L., LIU J., HU Y., *Surface plasmon resonance sensor based on dual-side polished microstructured optical fiber with dual-core*, Sensors **20**(14), 2020: 3911. https://doi.org/10.3390/s20143911

[25] ZHAO Q., LIU J., YANG H., LIU H., ZENG G., HUANG B., *High birefringence D-shaped germanium -doped photonic crystal fiber sensor*, Micromachines **13**(6), 2022: 826. https://doi.org/10.3390/mi13060826

[26] WANG Y., JIANG G., YU Z., WANG Q., JIANG X., *Trapezium-shaped groove photonic crystal fiber plasmon sensor for low refractive index detection*, Sensing and Bio-Sensing Research **34**, 2021: 100452. https://doi.org/10.1016/j.sbsr.2021.100452

[27] JI X., LUAN N., ZHANG W., QI Y., LUO M., LIU J., *Side-opening grapefruit fiber-based SPR sensor for simultaneous measurement of refractive index and temperature*, IEEE Photonics Journal **14**(6), 2022: 6859006. https://doi.org/10.1109/JPHOT.2022.3219137

[28] LIU Q., SUN J., SUN Y., LIU W., WANG F., YANG L., LIU C., LIU Q., LI Q., REN Z., SUN T., CHU P.K., *Surface plasmon resonance sensor based on eccentric core photonic quasi-crystal fiber with indium tin oxide*, Applied Optics **58**(25), 2019: 6848-6853. https://doi.org/10.1364/AO.58.006848

[29] CHU S., NAKKEERAN K., ABOBAKER A.M., APHALE S.S., BABU P.R., SENTHILNATHAN K., *Design and analysis of surface-plasmon-resonance-based photonic quasi-crystal fibre biosensor for high-refractive-index liquid analytes*, IEEE Journal of Selected Topics in Quantum Electronics **25**(2), 2019: 6900309. https://doi.org/10.1109/JSTQE.2018.2873481

[30] MANICKAM P., SENTHIL R., *Numerical demonstration of photonic quasi-crystal fiber–surface plasmonic resonance urinary methanol sensor*, Plasmonics **18**, 2023: 511-519. https://doi.org/10.1007/s11468-022-01768-8

[31] HUANG T., *Highly sensitive SPR sensor based on D-shaped photonic crystal fiber coated with indium tin oxide at near-infrared wavelength*, Plasmonics **12**, 2017: 583-588. https://doi.org/10.1007/s11468-016-0301-7

[32] SELLERI S., PETRÁČEK J., *Modal analysis of rib waveguide through finite element and mode matching methods*, Optical and Quantum Electronics **33**, 2001: 373-386. https://doi.org/10.1023/A:1010838716217

[33] CHEN N., CHANG M., ZHANG X., ZHOU J., LU X., ZHUANG S., *Highly sensitive plasmonic sensor based on a dual-side polished photonic crystal fiber for component content sensing applications*, Nanomaterials **9**(11), 2019: 1587. https://doi.org/10.3390/nano9111587

[34] LUAN N, WANG R, LV W, YAO J., *Surface plasmon resonance sensor based on D-shaped microstructured optical fiber with hollow core*, Optics Express **23**(7), 2015: 8576-8582. https://doi.org/10.1364/OE.23.008576

Received November 28, 2023
in revised form April 28, 2024